

dN/dx Reconstruction with Deep Learning for High-Granularity TPCs

Guang Zhao,^{a,1} Yue Chang,^b Jinxian Zhang,^{a,c} Linghui Wu,^a Huirong Qi,^a Xin She,^{a,c} Mingyi Dong,^{a,c} Shengsen Sun,^{a,c} Jianchun Wang,^a Yifang Wang,^a Chunxu Yu^d

^a*Institute of High Energy Physics, Chinese Academy of Sciences, Beijing*

^b*Central China Normal University, Wuhan, Hubei*

^c*University of Chinese Academy of Sciences, Beijing*

^d*Nankai University, Tianjin*

E-mail: zhaog@ihep.ac.cn

ABSTRACT: Particle identification (PID) is essential for future particle physics experiments such as the Circular Electron-Positron Collider and the Future Circular Collider. A high-granularity Time Projection Chamber (TPC) not only provides precise tracking but also enables dN/dx measurements for PID. The dN/dx method estimates the number of primary ionization electrons, offering significant improvements in PID performance. However, accurate reconstruction remains a major challenge for this approach. In this paper, we introduce a deep learning model, the Graph Point Transformer (GraphPT), for dN/dx reconstruction. In our approach, TPC data are represented as point clouds. The network backbone adopts a U-Net architecture built upon graph neural networks, incorporating an attention mechanism for node aggregation specifically optimized for point cloud processing. The proposed GraphPT model surpasses the traditional truncated mean method in PID performance. In particular, the K/π separation power improves by approximately 10% to 20% in the momentum interval from 5 to 20 GeV/c .

KEYWORDS: Particle Identification, Time Projection Chamber, Cluster Counting, dN/dx , Deep Learning, Point Cloud, Transformer

ARXIV EPRINT: [2510.10628](https://arxiv.org/abs/2510.10628)

¹Corresponding author.

Contents

1	Introduction	1
2	Detector Simulation and Data Samples	2
2.1	The CEPC TPC	2
2.2	Simulation Framework	3
2.3	Data Samples	4
3	Reconstruction with Truncated Mean Method	5
4	Reconstruction with Deep Learning	6
4.1	Related Works	6
4.2	Design Principle	7
4.3	Backbone Structure	7
4.4	Transformer Layer	8
4.5	Training	9
5	Performances	9
5.1	Parameter optimization	10
5.2	Classification Performance	11
5.3	PID Performance	12
6	Conclusion and Outlook	14

1 Introduction

Particle identification (PID) is a fundamental experimental technique in particle physics. At next-generation facilities such as the Circular Electron-Positron Collider (CEPC) [1, 2] and the Future Circular Collider (FCC-ee) [3], hadron identification is expected to remain effective up to momenta of several tens of GeV/c . Conventional dE/dx measurements in current gaseous detectors [4–7], which determine the total energy loss of a charged particle, cannot meet this requirement due to large fluctuations. Recent advances in electronics and detector technology now allow gaseous detectors to measure individual electron signals, enabling cluster counting (dN/dx). Unlike traditional dE/dx methods, the dN/dx method directly determines the number of primary ionization clusters [8, 9], thereby suppressing the impact of secondary ionization as well as fluctuations from energy loss and amplification, and thus offering a significant enhancement in PID performance.

The dN/dx method can be implemented in a Time Projection Chamber (TPC) when the readout granularity is sufficient to resolve individual electrons. Consequently, the baseline detector design for the CEPC features a large-volume, high-granularity TPC optimized for

dN/dx measurements [10, 11]. Reconstruction, however, presents a significant challenge. In a large-volume TPC such as that proposed for the CEPC, the detector length is 5.8 m, corresponding to a maximum electron drift distance of 2.9 m. Such a long drift distance results in transverse diffusion on the order of several hundred micrometers, which complicates the use of spatial locality to distinguish overlapping clusters. Furthermore, the CEPC TPC has a pad size of $500 \times 500 \mu\text{m}^2$ to balance performance and power consumption. With this pad size and a gas mixture of Ar:CF₄:iC₄H₁₀ (95:3:2), each pad collects on average about 1.8 primary electrons. Secondary electrons further increase this number, making dN/dx reconstruction particularly challenging.

These challenges make traditional rule-based reconstruction algorithms highly difficult. Deep learning, a statistical-based approach that leverages large training datasets, can extract complex features from the data. In this paper, we propose a dN/dx reconstruction algorithm based on deep neural networks, which demonstrates superior performance compared with traditional methods. The remainder of this paper is organized as follows: Section 2 introduces the detector simulation framework and data samples; section 3 describes the traditional truncated mean reconstruction method; section 4 details the deep-learning-based reconstruction algorithm; section 5 presents the performances; and section 6 provides the conclusion and plan.

2 Detector Simulation and Data Samples

2.1 The CEPC TPC

The CEPC TPC is contained within a cylindrical volume with an outer radius of 1.8 m, an inner radius of 0.6 m, and a total length of 5.8 m (figure 1). It operates in a 3 T magnetic field. A central cathode, held at a potential of -63 kV, divides the chamber into two drift regions. As charged particles pass through the detector, they ionize the gas mixture, and the liberated electrons drift toward the readout planes.

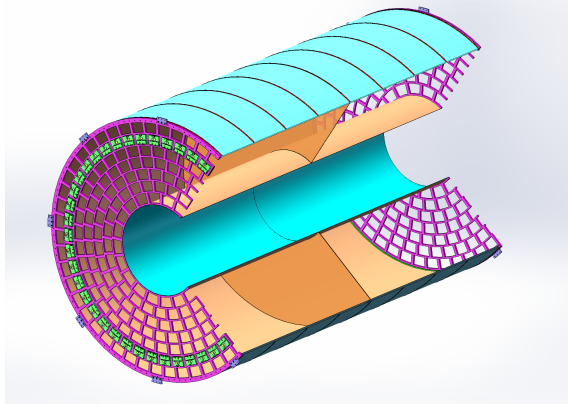


Figure 1. The CEPC TPC is a cylindrical, gas-filled tracking detector whose axis is aligned with the nominal beam direction. The barrel houses a field cage assembly that generates a uniform electric drift field along the Z-axis. Two readout endplates provide mechanical support for the barrel, while a central cathode plane is located at its mid-plane.

Each endcap is equipped with 244 readout modules. Each module consists of a MicroMegas detector [12], a readout pad plane and the associated readout electronics. The modules also integrate all necessary high- and low-voltage supply cables, along with a cooling system to dissipate heat generated by the electronics.

A high-granularity readout [13] with a pad size of $500 \times 500 \mu\text{m}^2$ was chosen based on simulation studies, with power consumption also taken into account. Each endcap contains more than 30 million readout channels in total. The fine granularity enables precise dN/dx measurements and has the potential to significantly enhance PID performance. The key design parameters of the CEPC TPC are summarized in table 1.

Table 1. Key parameters of the CEPC TPC.

Parameter	Value
Radial extension	0.6–1.8 m
Full length	5.8 m
Potential at cathode	-63,000 V
Gas mixture	Ar:CF ₄ :iC ₄ H ₁₀ = 95:3:2
Drift velocity	8 cm/ μs
Transverse diffusion	30 $\mu\text{m}/\sqrt{\text{cm}}$
Longitudinal diffusion	262 $\mu\text{m}/\sqrt{\text{cm}}$
Gas gain (MicroMegas)	2000
Pad size	$500 \times 500 \mu\text{m}^2$
Total readout modules (per endcap)	244
Total readout channels (per endcap)	$\sim 33.5 \text{ M}$
Equivalent Noise Charge (per channel)	$100 e^-$
Power consumption	< 100 mW/cm ²

2.2 Simulation Framework

The TPC simulation framework is built on Garfield++ [14, 15] with parameterizations that incorporate detector geometry, ionization processes, electron transport, electron amplification, and signal readout. The latter two stages are informed by results from existing prototype tests [13, 16, 17]. As illustrated in figure 2, a full TPC chamber is implemented in the simulation. The gas mixture is set to Ar:CF₄:iC₄H₁₀ (95:3:2). Ionization processes are simulated using the Heed code [18], which is widely employed for precise ionization modeling in gases.

Subsequent processes—electron transport, electron amplification and signal readout—are simulated using parameterized methods, since a full Garfield++ simulation would be computationally prohibitive. The drift velocity and diffusion coefficients of electrons are obtained from the full Garfield++ simulation. The uncertainties in drift position and timing as functions of drift distance are described by a square-root dependence. The final position and timing of each electron after transport are then determined through a sampling procedure. As shown in figure 3a, the primary and secondary electrons are dispersed around the track trajectory at the readout.

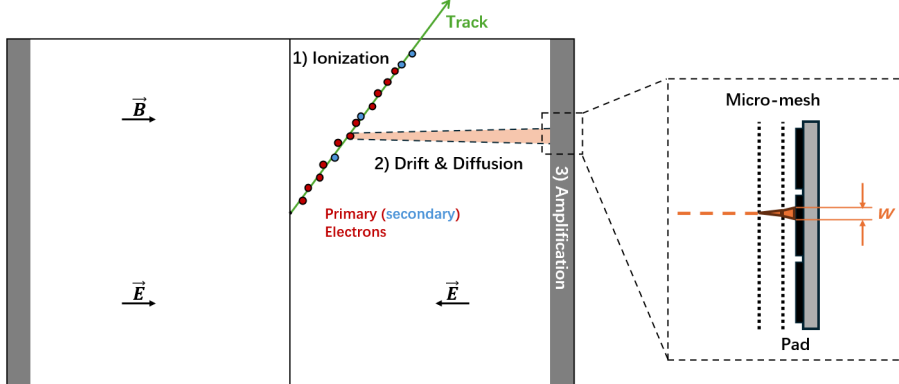


Figure 2. Working principle of a TPC. 1) As a charged particle traverses the TPC gas mixture, it generates a series of primary and secondary electrons. 2) These electrons drift toward the endcap under the influence of an electric field, undergoing diffusion during their transport. 3) Upon reaching the endcap, the electrons are amplified in the MicroMegas, producing a cluster whose spatial distribution has an effective width w .

The transported electrons are further amplified in the MicroMegas detector. The avalanche region of the MicroMegas provides a gain of 2000, and the single-electron gain distribution is modeled with a Polya function [19]. Within the framework, the number of electrons after amplification is sampled according to the Polya distribution, while the spatial density of the amplified electrons is described by a two-dimensional (2D) Gaussian distribution with an effective width w (within $\pm 3\sigma$) of approximately 100 μm .

Finally, the amplified signal is read out according to the pad geometry. Electronic noise is added to all pads using a Gaussian parameterization with a noise level of 100 e^- per channel. Figure 3b presents the final pad responses after accounting for all the processes described above.

2.3 Data Samples

Hadron samples are generated using the simulation framework. For the training dataset, 20,000 pion tracks and 20,000 kaon tracks are produced. These tracks are generated at a fixed polar angle of 60° with momenta ranging from 0.5 GeV/c to 20.5 GeV/c. For the testing dataset, hadron tracks are generated at fixed momenta and a fixed polar angle. The chosen momenta are 5 GeV/c, 10 GeV/c, 15 GeV/c, and 20 GeV/c, all at a polar angle of 60°, with 5,000 tracks generated for each momentum value.

Within the simulation framework, all pad-related hits are recorded for each simulated track. There is a one-to-one correspondence between hits and pads. For each hit, the deposited charge and timing information are stored, and its 2D position can be determined from the detector geometry. The charge and timing serve as input features for each hit, while the hit position is used to construct the point cloud representation. All input variables are normalized before being fed into the neural network.

In addition to these detector response data, the Monte Carlo (MC) truth information—essential for neural network training—is also included. For each pad, the number of primary

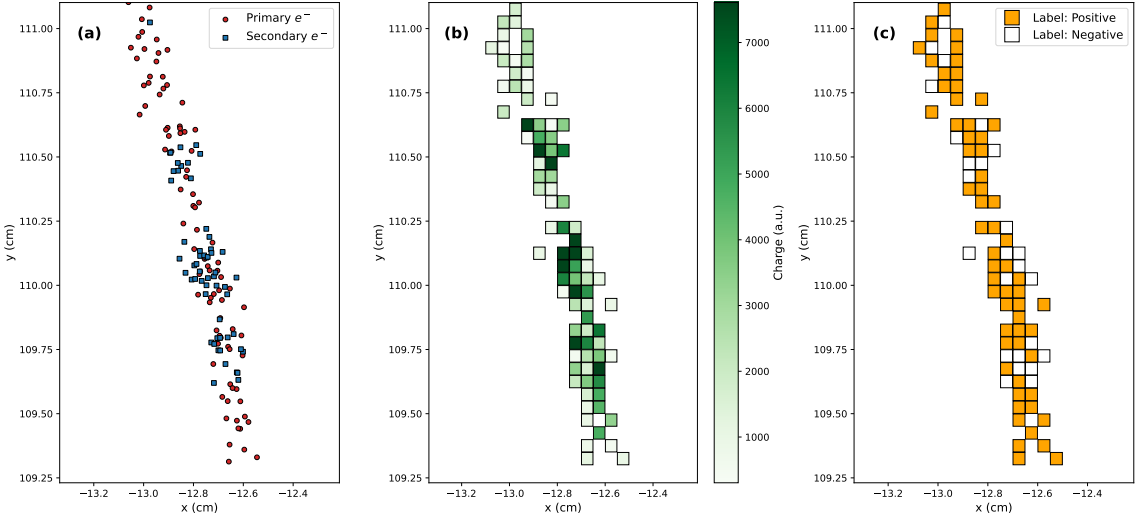


Figure 3. CEPC TPC readout responses for a 2 cm track segment at the endcap. (a) Electrons before amplification, where the red circles represent primary electrons and the blue boxes represent secondary electrons. (b) Energy depositions on the readout pads, with the color bar indicating the deposited charge. (c) Pad labels on the readout pads, where the orange and white colors correspond to labels of positive and negative, respectively.

electrons prior to amplification is stored. As shown in figure 3c, a pad is labeled positive if it contains at least one primary electron; otherwise, it is labeled negative.

3 Reconstruction with Truncated Mean Method

An efficient reconstruction algorithm is essential for the dN/dx method. The ultimate objective is to determine the number of primary electrons—reflecting the ionization characteristics of a charged particle—from the 2D readout pads. However, as noted in section 1, secondary electrons can also generate signals on the readout pads, thereby degrading the dN/dx resolution by producing a Landau tail. Consequently, the reconstruction algorithm must be capable of suppressing the influence of these secondary electrons.

A conventional approach for suppressing secondary-electron effects is the truncated mean method, which has been widely applied in dE/dx reconstruction [20]. In this approach, dE/dx —the energy deposition per unit track length—is used as the reconstruction variable. To mitigate resolution degradation caused by energy-loss fluctuations, typically N independent dE/dx measurements M are performed at multiple sampling points along the track within the TPC volume. For sufficiently large N , the resulting dE/dx distribution approaches a Landau distribution. Because of its long tail, the mean value of this distribution is not a reliable estimator of dE/dx . A more robust estimator is the truncated mean, in which the highest measurements—most likely associated with secondary electrons—are discarded. The truncated mean is defined as the average over the lowest n values of the

dE/dx measurements M :

$$\langle M \rangle_\alpha = \frac{1}{n} \sum_{i=1}^n M_i, \quad (3.1)$$

where $M_i \leq M_{i+1}$ for $i = 1, \dots, N-1$ and $\alpha = n/N$ is a fraction. The truncated mean dE/dx distribution is well approximated by a Gaussian. For dN/dx , the number of activated pads per unit track length serves as the ionization measurement, since it is approximately proportional to the number of ionization electrons. Consequently, the same truncated mean method can be applied.

4 Reconstruction with Deep Learning

Traditional rule-based approaches, such as the truncated mean method, rely heavily on human expertise and struggle to address the challenges outlined in section 1 for dN/dx reconstruction. In contrast, deep-learning-based methods can fully exploit detector information. A deep neural network, trained on large datasets, is capable of capturing hidden correlations among primary and secondary electrons as well as noise contributions. Therefore, we propose a deep-learning method, termed Graph Point Transformer (GraphPT), for dN/dx reconstruction.

4.1 Related Works

Self-attention and transformer. Self-attention enables tokens to attend to all others, efficiently modeling long-range dependencies [21]. Transformers stack self-attention and feed-forward layers for parallel sequence modeling, achieving state-of-the-art results in natural language processing and vision. Vision Transformers (ViT) extend this idea to images by treating patches as tokens, capturing both local and global structure, and outperforming Convolutional Neural Networks [22, 23] on large datasets [24, 25].

Point-based networks. Point-based networks adapt transformers to unordered three-dimensional (3D) point clouds by applying self-attention with positional encodings from coordinates, capturing both local geometry and global context. PointNet [26] directly consumes point clouds while preserving permutation invariance. PointNet++ [27] extends this with a hierarchical design that learns local features at multiple scales. Point Transformer (PT) [28] replaces fixed pooling with adaptive self-attention, weighting neighbors by feature similarity and relative position to better capture local and long-range dependencies. Several improved PT variants have since been proposed [29, 30].

Graph-based networks. Graph Neural Networks (GNNs) [31] model point clouds as graph nodes connected through neighborhood relations. This enables learning of both local geometry and global shape, making them effective for classification, segmentation, and object detection [32–35].

dN/dx reconstruction. Traditional rule-based approaches to dN/dx reconstruction have been explored in several studies [36–38]. More recently, pioneering works have applied neural networks to dN/dx reconstruction, particularly in drift chambers, where signals are recorded as one-dimensional waveforms. Long Short-Term Memory networks and Dynamic Graph Convolutional Neural Networks (DGCNNs) [32] have been applied to peak detection and clustering tasks with simulated data, achieving performance superior to traditional derivative-based and timing-based methods [39]. Furthermore, an innovative domain adaptation approach [40], leveraging optimal transport theory [41], has been developed and successfully applied to test beam data.

4.2 Design Principle

For the TPC, each hit provides both 2D positional information and timing data, which together can be transformed into a 3D spatial coordinate. Consequently, a TPC track can be naturally represented as a point cloud. Inspired by the PT, we adopt a U-Net-based hierarchical architecture as the backbone. In this work, we further extend the framework by representing the irregularly distributed hits in 3D space as graphs, where the attention mechanism from the original PT is incorporated into the node aggregation process. This integration of GNNs allows more effective feature learning within the point cloud representation.

For the dN/dx reconstruction, each TPC hit is labeled either as positive or negative according to the number of primary electrons it contains, as determined from the MC truth information. Building on previous approaches, we streamline the reconstruction by unifying the two-step procedure described in ref. [39] into a single model. In this formulation, the reconstruction task can be defined as either a node classification problem or, equivalently, a point cloud segmentation problem.

4.3 Backbone Structure

As shown in figure 4, the backbone of the network is a U-Net-based [42] hierarchical architecture, consisting of a U-shaped encoder–decoder with skip connections. To begin, a graph is constructed for each TPC track, where every TPC hit represented as a node. The node features include the hit’s charge and timing, and nodes are connected to their k nearest neighbors (k NN) based on Euclidean distance. The graph sequentially executes the hierarchical encoder and decoder.

Within the encoder, transitions down are performed by randomly dropping a fraction of nodes while projecting the features into a higher-dimension space. Conversely, in the decoder, transitions up are achieved through interpolation, with features mapped back into a lower-dimension space. At each transition, a new k NN graph is constructed. Skip connections link layers at corresponding hierarchical levels, ensuring information flow across the network. Additionally, each transition layer incorporates a transformer layer, which will be discussed in the following section. At the end of the decoder, the output graph contains the same number of nodes as the initial input graph. Finally, an Multilayer Perceptron (MLP) layer followed by a softmax layer produces probabilities in the range $[0, 1]$. The detailed network parameters are summarized in table 2.

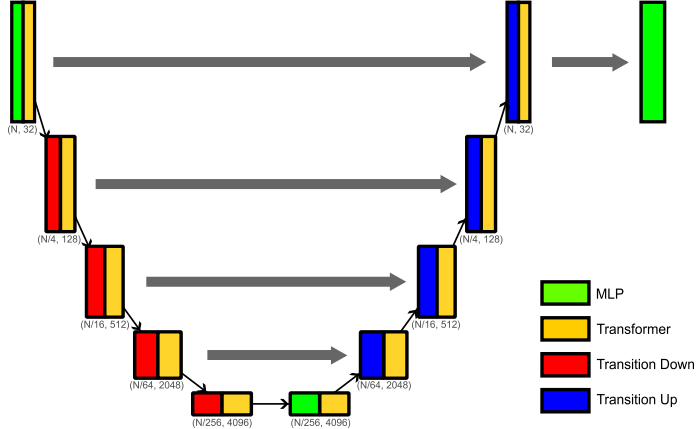


Figure 4. Backbone structure of the GraphPT. The network adopts a U-shaped encoder–decoder architecture with skip connections. Green boxes represent MLP layers, yellow boxes indicate transformer layers, red boxes correspond to transition-down layers, and blue boxes correspond to transition-up layers. Within the encoder, nodes are randomly dropped from the graph, and the features are projected into a higher-dimensional space. The decoder performs the inverse operation. Finally, an additional MLP layer is appended at the end of the U-Net.

Table 2. Parameters of GraphPT with transformer layers using subtraction and dot-product operators. In the table, d_{out} denotes the dimension of the output feature.

Network Parameter		GraphPT (Sub.)	GraphPT (Dot-prod.)
Feature Dimension	Input	2	2
	Encoder	[32, 128, 512, 2048, 8192]	[4, 16, 64, 256, 1024]
	Decoder	[8192, 2048, 512, 128, 32]	[1024, 256, 64, 16, 4]
	Output	1	1
Graph Construction	k in k NN graph	16	16
	Trans. down (up) ratio	0.25 (4)	0.25 (4)
Transformer Layer	Number of heads	—	8
	Attention network δ	MLP([d_{out} , 64, d_{out}])	—
	Positional network θ	MLP([3, 64, d_{out}])	MLP([3, 64, 64, d_{out}])

4.4 Transformer Layer

The core component of the GraphPT architecture is the transformer layer. In the context of GNNs, the transformer layer performs message-passing mechanism: each node aggregates information from its neighbors to update its own representation. Formally, the message-passing can be expressed as:

$$\mathbf{x}'_i = \beta(\mathbf{x}_i) + \sum_{j \in \mathcal{N}(i)} \alpha(\mathbf{x}_i, \mathbf{x}_j) \beta(\mathbf{x}_j), \quad (4.1)$$

where i denotes the index of the aggregation node with feature vector \mathbf{x}_i and $\mathcal{N}(i)$ represents its neighboring nodes. The function β maps the original feature vectors into a latent space, while the function α computes the attention weights used to aggregate neighbor information.

The attention weights are defined as:

$$\alpha(\mathbf{x}_i, \mathbf{x}_j) = \text{softmax}(\gamma(\mathbf{x}_i, \mathbf{x}_j)), \quad (4.2)$$

where γ is an operator that relates \mathbf{x}_i and \mathbf{x}_j . In this paper, two operators are investigated for the dN/dx reconstruction.

Subtraction operator. The first operator is the subtraction operator that is used in PT [28], which is defined as:

$$\gamma(\mathbf{x}_i, \mathbf{x}_j) = \delta(\phi(\mathbf{x}_i) - \psi(\mathbf{x}_j) + \theta(\mathbf{p}_i - \mathbf{p}_j)), \quad (4.3)$$

where ϕ and ψ are neural networks that transform the input features, θ is a positional embedding network that encodes the relative positional differences between a central node and its neighbors, and δ is a neural network that integrates these components into a unified representation.

Dot-product operator. In contrast, the second operator is proposed in this work as a novel alternative. Specifically, the dot-product operator, which constitutes the fundamental mathematical component underlying self-attention, is adapted to the dN/dx reconstruction. It is defined as:

$$\gamma(\mathbf{x}_i, \mathbf{x}_j) = \frac{\phi(\mathbf{x}_i)^\top (\psi(\mathbf{x}_j) + \theta(\mathbf{p}_i - \mathbf{p}_j))}{\sqrt{d_{\text{out}}}}, \quad (4.4)$$

where d_{out} denotes the dimensionality of the output tensor. In addition, the multi-head mechanism is incorporated, executing the attention operation multiple times in parallel, each with its own set of learned projections for queries, keys, and values, and concatenating the outputs of all heads. This design enables the model to capture long-range dependencies and subtle patterns, yielding richer and more expressive representations than the one with the subtraction operator.

4.5 Training

In this study, end-to-end training is performed, as perfect labels are available from the full MC simulation. A pad is labeled as positive if it is activated by one or more electrons; otherwise, it is labeled as negative. The neural network outputs a probability for each pad, and binary cross-entropy is employed as the loss function.

Network training is performed with the AdamW optimizer [43], combined with a decaying learning rate schedule. For the model with the subtraction operator, the learning rate decreases from 10^{-3} to 10^{-5} over 120 epochs. For the model with the dot-product operator, it decreases from 10^{-4} to 10^{-6} over 240 epochs.

5 Performances

The performance is evaluated using the testing dataset described in section 2.3. These samples are generated independently from those used in neural network training. We first optimize the algorithm parameters, then compute the metrics for the binary classification task, and finally present the resulting PID performance.

5.1 Parameter optimization

For the truncated mean method, two free parameters must be optimized. The first is the fraction α , typically chosen between 0.50 and 0.85. The second is the number of pad rows combined into a single measurement M . In a high-granularity TPC, using only one pad row per sample can introduce large fluctuations, whereas combining an appropriate number of pad rows improves stability. In practice, one of these two parameters is optimized while the other is kept fixed, according to the separation power of two particles A and B , which is defined as:

$$S_{A,B} = \frac{|\mu_A - \mu_B|}{\sqrt{(\sigma_A^2 + \sigma_B^2)/2}}, \quad (5.1)$$

where $\mu_{A(B)}$ and $\sigma_{A(B)}$ are the measured dE/dx or dN/dx and its resolution for particle $A(B)$, respectively. As shown in figure 5, the optimal fraction α is 0.65, with two pad rows combined.

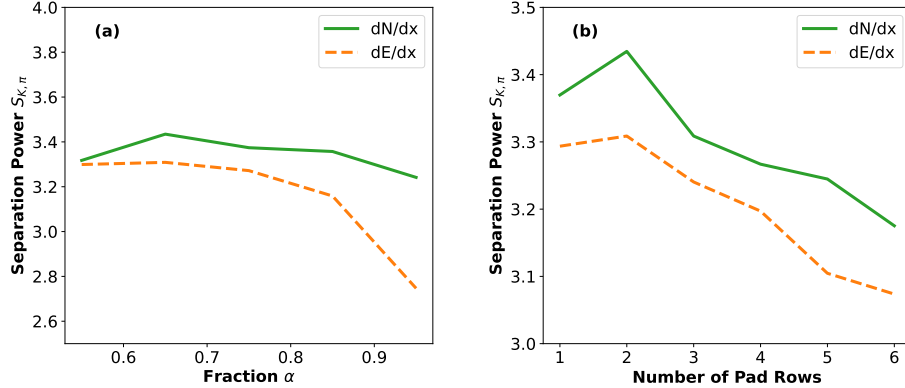


Figure 5. Optimization of the truncated mean method using 20 GeV/c samples. (a) The K/π separation power as a function of the fraction α , with the number of pad rows fixed to two. (b) The K/π separation power as a function of the number of pad rows to be combined, with the fraction fixed at $\alpha = 0.65$. The green solid line represents the dN/dx method, while the orange dashed line represents the dE/dx method. The optimal values are $\alpha = 0.65$ and two pad rows, respectively.

For the GraphPT, the neural network outputs a probability p_i for each TPC hit. These probabilities are then used for the dN/dx reconstruction, which is defined as:

$$dN/dx = \frac{1}{L} \sum_{i=1}^N \mathbf{1}_{\{p_i > \tau\}}, \quad (5.2)$$

where i denotes the hit index, $\mathbf{1}$ is the indicator function, τ is a threshold, and L is the track length. The threshold τ must be optimized according to the separation power. Figure 6 illustrates the K/π separation power as a function of the threshold. The optimal values are 0.157 and 0.261 for the GraphPT with the subtraction operator and dot-product operator, respectively.

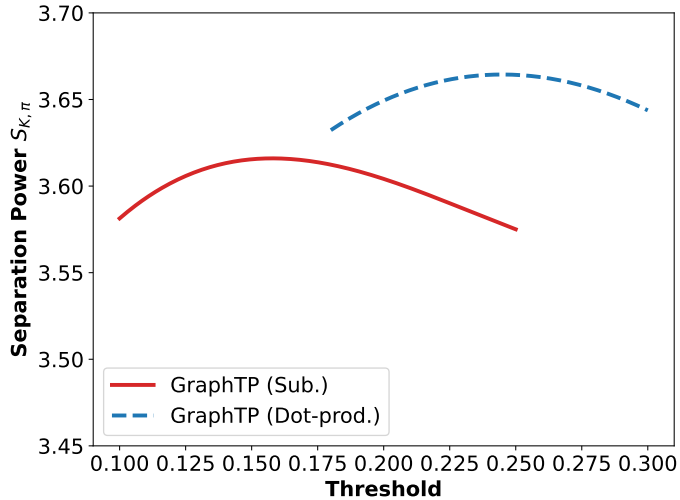


Figure 6. Threshold optimization in GraphPT using 20 GeV/c samples. The red solid line shows the GraphPT using the subtraction operator, while the blue dashed line corresponds to the GraphPT with the dot-product operator. The respective optimal thresholds are 0.157 and 0.261.

5.2 Classification Performance

With the optimized parameters, dN/dx reconstruction is carried out using both the truncated mean method and the GraphPT model. Figure 7 shows an example of the classification result for the track segment shown in figure 3: pads marked as circles (for the GraphPT) or stars (for the truncated mean) are classified as negatives (secondary electrons), while all other pads are classified as positives (primary electrons). Examination of the zoomed-in region in figure 7b reveals that the GraphPT model produces almost no false-negatives, whereas the truncated mean method is more aggressive and results in several false-negatives, as illustrated in figure 7c, which can reduce signal efficiency.

The classification performance is further validated on the full testing samples using the two widely adopted evaluation metrics: accuracy and the F1-score. Accuracy measures the proportion of correct predictions out of all predictions, making it a intuitive and widely applicable metric. It is defined as:

$$\text{Accuracy} = \frac{\text{TP} + \text{TN}}{\text{TP} + \text{TN} + \text{FP} + \text{FN}}, \quad (5.3)$$

where the TP, TN, FP, FN denote the numbers of true positives, true negatives, false positives and false negatives, respectively. The F1-score, by contrast, is the harmonic mean of precision and recall, capturing the balance between correctly identifying positive cases and avoiding false alarms:

$$\text{F1-Score} = 2 \times \frac{P \times R}{P + R}, \quad (5.4)$$

where P denotes precision ($\text{TP} / (\text{TP} + \text{FP})$) and R denotes recall ($\text{TP} / (\text{TP} + \text{FN})$).

Table 3 presents the results obtained with different reconstruction methods. Relative to the truncated mean approach, the GraphPT models yield lower precision but substantially

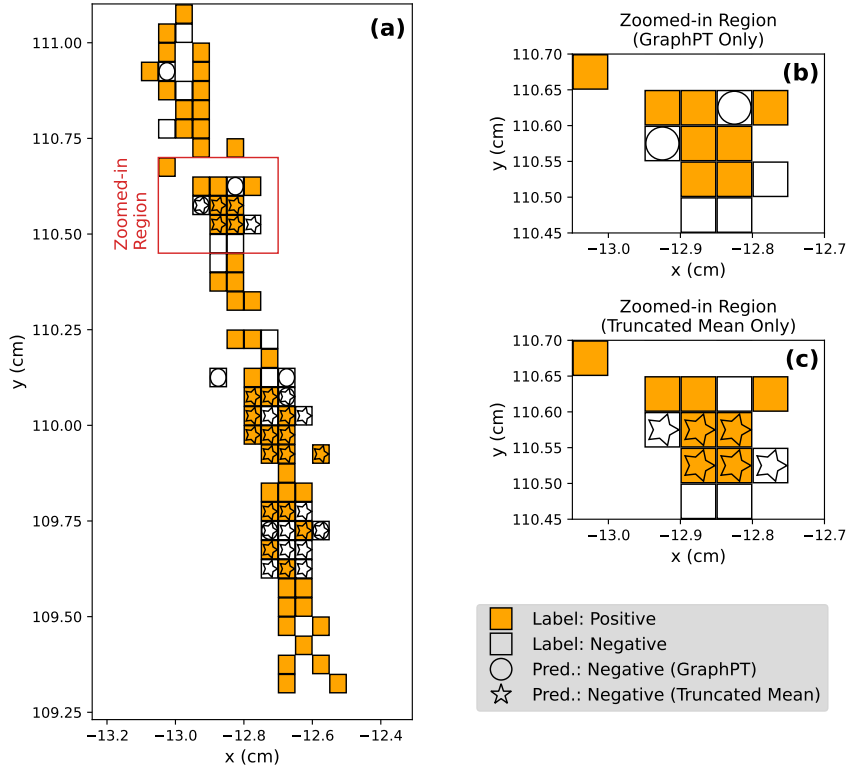


Figure 7. Predicted pad classes for the same track segment shown in figure 3. (a) Pads predicted as negatives are marked by circles for the GraphPT and stars for the truncated mean method, respectively; all other pads are predicted as positives. The red box highlights the zoomed-in region. (b) The zoomed-in region using only the GraphPT method. (c) The zoomed-in region using only the truncated mean method.

higher recall, indicating markedly improved signal efficiency at the cost of slightly reduced purity. This observation is consistent with the behavior illustrated in figure 7. In terms of overall classification performance—assessed by accuracy and F1-score—the GraphPT models clearly surpass the traditional truncated mean method. Among the two GraphPT variants, the model incorporating the dot-product operator achieves slightly superior classification performance.

Table 3. Classification metrics.

Method	Accuracy	Precision	Recall	F1-Score
Truncated Mean	0.601	0.743	0.574	0.648
GraphPT (Sub.)	0.698	0.689	0.960	0.802
GraphPT (Dot-prod.)	0.707	0.702	0.941	0.804

5.3 PID Performance

The PID performance is further evaluated using the particle separation power defined in eq. 5.1. Figure 8 presents the K/π separation $S_{K,\pi}$ as a function of track momentum.

The tracks originate from the collision point with a polar angle of 60° , corresponding to a track length of approximately 1.4 m. For the dN/dx results (shown in red circulars), the conclusions are consistent with those in table 3: the GraphPT method significantly enhances PID performance compared to the traditional truncated mean approach, with the dot-product operator yielding the best overall K/π separation. Specifically, the improvements range from approximately 10% (5%) to 20% (15%) in the momentum interval from 5 to 20 GeV/c for the dot-product (subtraction) operator.

For comparison, dE/dx results obtained with pad sizes of $500 \times 500 \mu\text{m}^2$ and $6 \times 1 \text{ mm}^2$ are also shown (shown in blue rectangles), with the latter representing a conventional large-pad readout. As expected, all dN/dx results outperform those from dE/dx . Moreover, the PID performance achieved with dN/dx is even superior when compared to dE/dx obtained using the conventional large-pad readout.

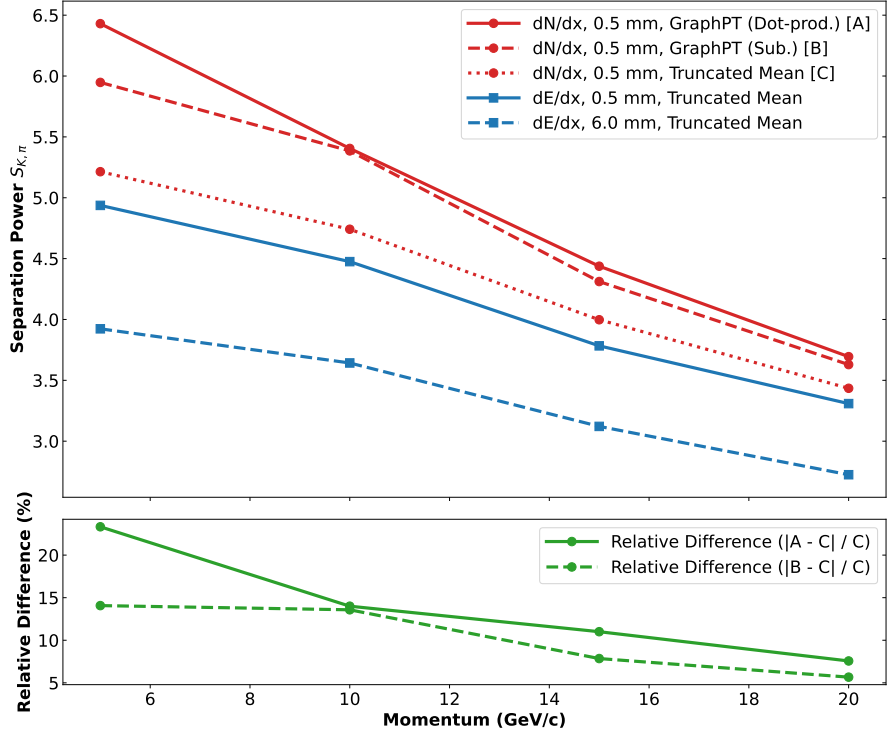


Figure 8. K/π separation power as a function of particle momentum. Red lines with circular markers denote the dN/dx results, while blue lines with rectangular markers correspond to the dE/dx results. For the red curves, the solid line shows the GraphPT model with a subtraction operator, the dashed line represents the GraphPT model with a dot-product operator, and the dotted line indicates the traditional truncated mean method. For the blue curves, the solid and dashed lines correspond to dE/dx results obtained with the truncated mean method for pad lengths of $500 \mu\text{m}$ and 6 mm , respectively. The relative differences between the GraphPT model with a dot-product (subtraction) operator and the truncated mean dN/dx are shown by the solid (dashed) green line.

6 Conclusion and Outlook

In this paper, we propose a general deep-learning-based dN/dx reconstruction approach, GraphPT, for high-granularity TPCs. The TPC data are represented as point clouds. The network backbone employs a U-Net architecture built upon GNNs, incorporating an attention mechanism for node aggregation specifically tailored to point cloud processing. The model is optimized for the CEPC TPC and trained on hadron samples generated with a sophisticated simulation framework that provides detailed detector simulation and digitization.

By evaluating both the classification and PID performances, we find that the GraphPT model achieves superior results. Compared with the traditional truncated mean method, the GraphPT model serves as a substantially more powerful classifier, delivering higher accuracy and F1-score. The K/π separation power improves by approximately 10% (5%) to 20% (15%) in the momentum interval from 5 to 20 GeV/c when using dot-product (subtraction) operators. Relative to the conventional dE/dx method for the current-generation detector, the improvement is even larger, reaching nearly 50%.

Looking ahead, several aspects require further study. First, the GraphPT model itself still needs optimization in terms of network architecture and hyperparameters. Second, in this work the model was trained on a fix-angle sample; future studies should extend the training to much larger and more diverse datasets. This will also necessitate improving the computational efficiency of the model to enable large-scale training.

The ultimate goal of this study is to access the feasibility of PID performance using the dN/dx method. To this end, further validation against detector R&D is essential. For the CEPC TPC, two TPC prototypes have already been designed. Beam tests are planned to evaluate their performance and provide experimental validation of the high-granularity readout approach. One such beam test has scheduled at Deutsches Elektronen-Synchrotron (DESY) [44], within the LCTPC Collaboration and the CERN R&D Collaboration on gaseous detector (DRD1) [45].

Acknowledgments

This research was funded by National Natural Science Foundation of China (NSFC) under Contract Nos. 12475200 and Nos. 12475192. We sincerely thank Tianchi Zhao for the helpful discussions and his valuable suggestions.

References

- [1] C.S. Group et al., *Cepc conceptual design report: Volume 2-physics & detector*, *arXiv preprint arXiv:1811.10545* (2018) .
- [2] J. Gao, *Cepc technical design report: accelerator, Radiation Detection Technology and Methods* **8** (2024) 1.
- [3] A. Blondel and P. Janot, *Fcc-ee overview: new opportunities create new challenges*, *The European Physical Journal Plus* **137** (2022) 92.

- [4] B. Collaboration et al., *The construction of the besiii experiment, Nuclear Instruments and Methods in Physics Research Section A: Accelerators, Spectrometers, Detectors and Associated Equipment* **598** (2009) 7.
- [5] T. Abe, I. Adachi, K. Adamczyk, S. Ahn, H. Aihara, K. Akai et al., *Belle ii technical design report, arXiv preprint arXiv:1011.0352* (2010) .
- [6] J. Alme, Y. Andres, H. Appelshäuser, S. Bablok, N. Bialas, R. Bolgen et al., *The alice tpc, a large 3-dimensional tracking device with fast readout for ultra-high multiplicity events, Nuclear Instruments and Methods in Physics Research Section A: Accelerators, Spectrometers, Detectors and Associated Equipment* **622** (2010) 316.
- [7] M. Anderson, J. Berkovitz, W. Betts, R. Bossingham, F. Bieser, R. Brown et al., *The star time projection chamber: a unique tool for studying high multiplicity events at rhic, Nuclear Instruments and Methods in Physics Research Section A: Accelerators, Spectrometers, Detectors and Associated Equipment* **499** (2003) 659.
- [8] V. Davidenko, B. Dolgoshein and S. Somov, *A translation of the zhurnal eksperimental'noi i teoreticheskoi fiziki, Zh. Eksp. Teor. Fiz.* **56** (1969) 3.
- [9] G. Cataldi, F. Grancagnolo and S. Spagnolo, *Cluster counting in helium based gas mixtures, Nuclear Instruments and Methods in Physics Research Section A: Accelerators, Spectrometers, Detectors and Associated Equipment* **386** (1997) 458.
- [10] Y. Chang, H. Qi, X. She, C. Yu, J. Zhang, H. Dai et al., *Feasibility study of the pixel readout tpc technology at high luminosity tera z on cepc*, .
- [11] Y. Zhu, S. Chen, H. Cui and M. Ruan, *Requirement analysis for de/dx measurement and pid performance at the cepc baseline detector, Nuclear Instruments and Methods in Physics Research Section A: Accelerators, Spectrometers, Detectors and Associated Equipment* **1047** (2023) 167835.
- [12] Y. Giomataris, P. Reboursard, J.P. Robert and G. Charpak, *Micromegas: a high-granularity position-sensitive gaseous detector for high particle-flux environments, Nuclear Instruments and Methods in Physics Research Section A: Accelerators, Spectrometers, Detectors and Associated Equipment* **376** (1996) 29.
- [13] C. Liu, Y. Yang, Z. Deng, G. Gong, J. Dong, H. Qi et al., *Development of an interposer based pixel readout for cepc tpc, Journal of Instrumentation* **20** (2025) C08006.
- [14] H. Schindler and R. Veenhof, “Garfield++: Simulation of tracking detectors.” <https://garfieldpp.docs.cern.ch/>.
- [15] R. Veenhof et al., *Garfield, a drift chamber simulation program*, in *Conf. Proc. C*, vol. 9306149, pp. 66–71, World Scientific, 1993.
- [16] Z. Zhang, B. Qi, M. Shao, J. Feng, X. Wang, C. Liu et al., *Study on the double micro-mesh gaseous structure (dmm) as a photon detector, Nuclear Instruments and Methods in Physics Research Section A: Accelerators, Spectrometers, Detectors and Associated Equipment* **952** (2020) 161978.
- [17] Y. Chang, H. Qi, X. She, J. Zhang, C. Yu, Z. Yuan et al., *Design and commission of tpc prototype integrated with 266 nm uv laser, Journal of Instrumentation* **20** (2025) P02025.
- [18] I.B. Smirnov, *Modeling of ionization produced by fast charged particles in gases, Nuclear Instruments and Methods in Physics Research Section A: Accelerators, Spectrometers, Detectors and Associated Equipment* **554** (2005) 474.

- [19] G. Pólya, *Sur quelques points de la théorie des probabilités*, in *Annales de l'institut Henri Poincaré*, vol. 1, pp. 117–161, 1930.
- [20] C. Lippmann, *Particle identification, Nuclear Instruments and Methods in Physics Research Section A: Accelerators, Spectrometers, Detectors and Associated Equipment* **666** (2012) 148.
- [21] A. Vaswani, N. Shazeer, N. Parmar, J. Uszkoreit, L. Jones, A.N. Gomez et al., *Attention is all you need*, *Advances in neural information processing systems* **30** (2017) .
- [22] A. Krizhevsky, I. Sutskever and G.E. Hinton, *Imagenet classification with deep convolutional neural networks*, *Advances in neural information processing systems* **25** (2012) .
- [23] Y. LeCun, B. Boser, J.S. Denker, D. Henderson, R.E. Howard, W. Hubbard et al., *Backpropagation applied to handwritten zip code recognition*, *Neural computation* **1** (1989) 541.
- [24] A. Dosovitskiy, L. Beyer, A. Kolesnikov, D. Weissenborn, X. Zhai, T. Unterthiner et al., *An image is worth 16x16 words: Transformers for image recognition at scale*, *arXiv preprint arXiv:2010.11929* (2020) .
- [25] K. Kim, B. Wu, X. Dai, P. Zhang, Z. Yan, P. Vajda et al., *Rethinking the self-attention in vision transformers*, in *Proceedings of the IEEE/CVF conference on computer vision and pattern recognition*, pp. 3071–3075, 2021.
- [26] C.R. Qi, H. Su, K. Mo and L.J. Guibas, *Pointnet: Deep learning on point sets for 3d classification and segmentation*, in *Proceedings of the IEEE conference on computer vision and pattern recognition*, pp. 652–660, 2017.
- [27] C.R. Qi, L. Yi, H. Su and L.J. Guibas, *Pointnet++: Deep hierarchical feature learning on point sets in a metric space*, *Advances in neural information processing systems* **30** (2017) .
- [28] H. Zhao, L. Jiang, J. Jia, P.H. Torr and V. Koltun, *Point transformer*, in *Proceedings of the IEEE/CVF international conference on computer vision*, pp. 16259–16268, 2021.
- [29] X. Wu, Y. Lao, L. Jiang, X. Liu and H. Zhao, *Point transformer v2: Grouped vector attention and partition-based pooling*, *Advances in Neural Information Processing Systems* **35** (2022) 33330.
- [30] X. Wu, L. Jiang, P.-S. Wang, Z. Liu, X. Liu, Y. Qiao et al., *Point transformer v3: Simpler faster stronger*, in *Proceedings of the IEEE/CVF conference on computer vision and pattern recognition*, pp. 4840–4851, 2024.
- [31] F. Scarselli, M. Gori, A.C. Tsoi, M. Hagenbuchner and G. Monfardini, *The graph neural network model*, *IEEE transactions on neural networks* **20** (2008) 61.
- [32] Y. Wang, Y. Sun, Z. Liu, S.E. Sarma, M.M. Bronstein and J.M. Solomon, *Dynamic graph cnn for learning on point clouds*, *ACM Transactions on Graphics (tog)* **38** (2019) 1.
- [33] W. Shi and R. Rajkumar, *Point-gnn: Graph neural network for 3d object detection in a point cloud*, in *Proceedings of the IEEE/CVF conference on computer vision and pattern recognition*, pp. 1711–1719, 2020.
- [34] D. Li, C. Lu, Z. Chen, J. Guan, J. Zhao and J. Du, *Graph neural networks in point clouds: A survey*, *Remote Sensing* **16** (2024) 2518.
- [35] Q. Zheng, Y. Qi, C. Wang, C. Zhang and J. Sun, *Pointvig: A lightweight gnn-based model for efficient point cloud analysis*, *arXiv preprint arXiv:2407.00921* (2024) .
- [36] J.-F. Caron, C. Hearty, P. Lu, R. So, R. Cheaib, J.-P. Martin et al., *Improved particle identification using cluster counting in a full-length drift chamber prototype*, *Nuclear*

Instruments and Methods in Physics Research Section A: Accelerators, Spectrometers, Detectors and Associated Equipment **735** (2014) 169.

- [37] C. Caputo, G. Chiarello, A. Corvaglia, F. Cuna, B. D’Anzi, N. De Filippis et al., *Particle identification with the cluster counting technique for the idea drift chamber*, *Nuclear Instruments and Methods in Physics Research Section A: Accelerators, Spectrometers, Detectors and Associated Equipment* **1048** (2023) 167969.
- [38] Y. Aoki, D. Attié, T. Behnke, A. Bellerive, O. Bezshyyko, D. Bhattacharya et al., *Double-hit separation and dE/dx resolution of a time projection chamber with gem readout*, *Journal of Instrumentation* **17** (2022) P11027.
- [39] Z.-F. Tian, G. Zhao, L.-H. Wu, Z.-Y. Zhang, X. Zhou, S.-T. Xin et al., *Cluster counting algorithm for the cepc drift chamber using lstm and dgcn*, *Nuclear Science and Techniques* **36** (2025) 113.
- [40] G. Zhao, L. Wu, F. Grancagnolo, N. De Filippis, M. Dong and S. Sun, *Peak finding algorithm for cluster counting with domain adaptation*, *Computer Physics Communications* **300** (2024) 109208.
- [41] L.V. Kantorovich, *On the translocation of masses*, in *Dokl. Akad. Nauk. USSR (NS)*, vol. 37, pp. 199–201, 1942.
- [42] O. Ronneberger, P. Fischer and T. Brox, *U-net: Convolutional networks for biomedical image segmentation*, in *International Conference on Medical image computing and computer-assisted intervention*, pp. 234–241, Springer, 2015.
- [43] I. Loshchilov and F. Hutter, *Decoupled weight decay regularization*, *arXiv preprint arXiv:1711.05101* (2017) .
- [44] R. Diener, J. Dreyling-Eschweiler, H. Ehrlichmann, I.-M. Gregor, U. Kötz, U. Krämer et al., *The desy ii test beam facility*, *Nuclear Instruments and Methods in Physics Research Section A: Accelerators, Spectrometers, Detectors and Associated Equipment* **922** (2019) 265.
- [45] A. Colaleo, L. Ropelewski, M. Gouzevitch, M. Tytgat, A. Delbart, G. Croci et al., *Drd1 extended r&d; proposal*, Tech. Rep. (2024).